Title
Predicting supercooling of phase change materials in arbitrarily varying conditions

Journal
Cell Reports Physical Science, 4(6)

ISSN
2666-3864

Authors
Song, Youngsup
Lilley, Drew
Chalise, Divya
et al.

Publication Date
2023-06-01

DOI
10.1016/j.xcrp.2023.101462

Peer reviewed

Predicting Supercooling of Phase Change Materials in Arbitrarily Varying Conditions

Youngsup Song[1], Drew Lilley[1,2], Divya Chalise[1,2], Sumanjeet Kaur[1], Ravi S. Prasher[1,2*]*

[1]Energy Technologies Area, Lawrence Berkeley National Laboratory, Berkeley, CA 94720, USA
[2]Department of Mechanical Engineering, University of California, Berkeley, CA 94720, USA

*Correspondence: mailto:skaur1@lbl.gov and rsprasher@lbl.gov

SUMMARY

Phase change materials (PCMs) are promising for thermal energy storage; however, one major bottleneck for their practical implementation has been their unclear supercooling behaviors. In this work, we introduce a framework to predict the degree of supercooling for a PCM with arbitrary geometrical and thermal conditions by analyzing the PCM's intrinsic nucleation characteristics with a statistical model. The prediction capability of our framework was successfully validated with experiments using magnesium chloride hexahydrate as a PCM. For a system with a uniform temperature distribution, our framework could predict the average degree of supercooling. For a general case such as PCM embedded in a heat sink, the framework could accurately predict the expected time for nucleation for given conditions combined with numerical simulations. This work provides important insights in understanding and predicting the supercooling behavior of PCMs, thereby providing guidelines for the optimal design of PCM-based thermal energy storage applications.

KEYWORDS

Energy storage, Thermal storage, Heat battery, Magnesium chloride hexahydrate, Salt hydrates, Fatty acids, Nucleation

INTRODUCTION

With roughly half of global energy being used as heat for buildings and industrial processes,[1] thermal energy storage (TES) technologies will play a pivotal role for the deep decarbonization of heat. TES also has potential for grid-scale power supply with its low cost and superior scalability compared to electrochemical batteries.[2] In addition to heat and power supply, TES has immense utility in thermal management of high-power-density applications, e.g., batteries,[3] electronics,[4] and photovoltaics.[5] Phase change materials (PCM) in particular are very attractive due to high energy density and low cost.[6] Despite the affordable cost, scalability, and urgent need for PCM-based TES in a variety of energy applications, the practical implementation of PCM-based TES has fallen behind compared to other energy storage technologies. A major technical reason limiting the implementation is a supercooling phenomenon of PCMs.

PCMs are widely investigated materials for TES, and they charge and discharge heat by harnessing the latent heat of phase change.[7,8] When PCMs cool down, they often freeze at a lower temperature than their thermodynamic equilibrium melting temperature. This phenomenon is called supercooling, also known as subcooling or undercooling, and the degree of supercooling (θ_s) can be expressed as the difference between the melting (T_m) and freezing (T_f) temperatures, i.e., $\theta_s = T_m - T_f$. The accurate prediction of θ_s is critical for the design of PCM-based TES systems. If a PCM cools below T_m but does not reach T_f, for example, the PCM will stay as a liquid and the system will fail to exploit the large latent heat of fusion stored in the PCM; instead, only the small fraction of sensible heat will discharge. Several types of PCMs, including salt hydrates,[9] sugar alcohols,[10] and metals,[11,12] are particularly prone to the significant supercooling phenomenon. This is due to their slow nucleation kinetics or large nucleation energy barriers resulting from their unique molecular structures.

PCM properties such as T_m and heat capacity (c_p) can be accurately characterized by a lab-scale analysis using differential scanning calorimetry (DSC), in which a less than 100 μL sample is used for the measurement (**Figure 1a**). θ_s, on the other hand, is an extrinsic property that highly depends on the volume of a PCM because the number of nucleation sites scales with volume, which may alter θ_s. In fact, the significant difference in scales between TES applications, e.g., building envelopes with embedded PCMs larger than 1 L (Figure 1b), and lab-scale DSC samples

less than 100 μL (Figure 1a) makes the θ_s measured by the lab-scale DSC almost meaningless for actual TES applications. θ_s also highly depends on thermal boundary conditions that determine the temperature distribution in the PCM. For a DSC sample, due to its small volume, we can assume a lumped condition for most cases, i.e., spatially uniform temperature distribution, such that the Biot number ($Bi = \frac{hL}{k}$) is smaller than 0.1 (Figure 1a), where h, L, and k are the heat transfer coefficient, length scale of PCM, and thermal conductivity of PCM, respectively. Here, L can be evaluated as the ratio of volume (V) to surface area (A). For most system-scale PCMs, on the other hand, their scale makes the Bi much larger than 0.1, and thus, the temperature distribution in the PCM is non-uniform. This temperature non-uniformity makes the evaluation of θ_s in system-scale PCMs trickier (Figure 1b). The effects of scale on θ_s can be found in Figure 1c, where we plotted θ_s of one widely investigated PCM, magnesium chloride hexahydrate ($MgCl_2 \cdot 6H_2O$), using data obtained from the literature, as a function of volume.[13-23] The plot includes the data measured by DSC (blue circles) and in an oven with larger volumes (red squares). Indeed, θ_s decreases as volume increases. θ_s varies significantly, however, even for similar volumes, which shows the effects of the material's purity or different thermal conditions that the samples are subject to. This basically translates into the fact that $\theta_s = f(V, \Delta T)$ where ΔT represents the temperature gradient in the system. ΔT is a function of V as well as thermal properties and thermal boundary condition. The coupled effects of scale and thermal conditions on θ_s has made the prediction of θ_s notoriously challenging. Various techniques have been investigated to lower θ_s by adding nucleating agents into PCMs, mixing different types of PCMs or applying external fields.[9,24-26] While such efforts reduce θ_s to some extent, supercooling and its stochastic nature still exist, indicating the greater importance of understanding supercooling and predicting θ_s.

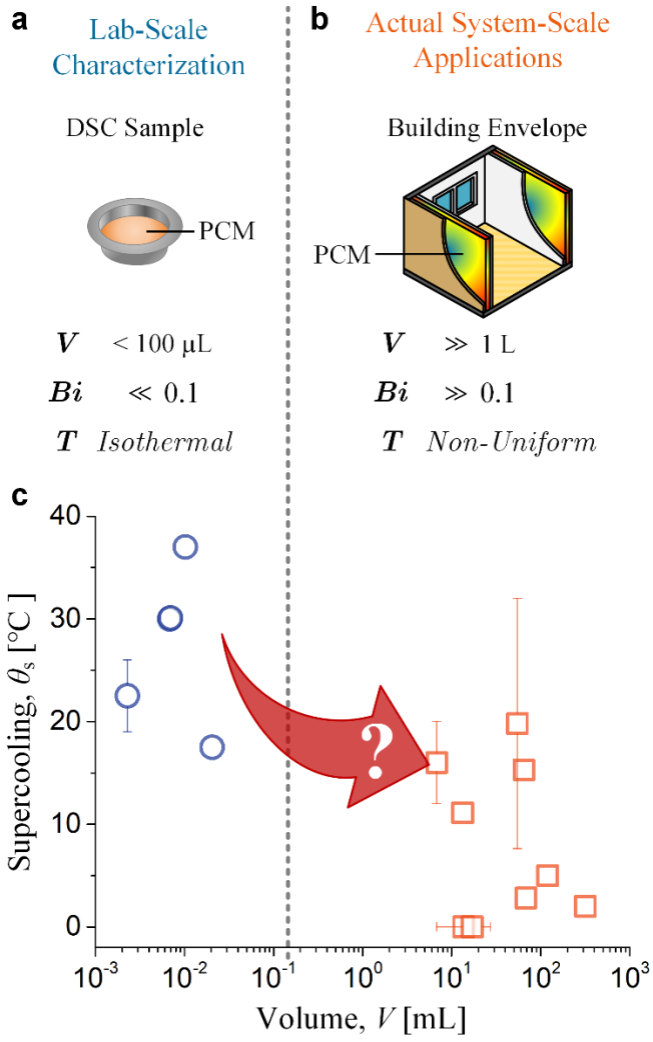

Figure 1. Differences in experimental conditions for lab-scale and system-scale PCMs that affect the degree of supercooling (θ_s) of a PCM. (a) A schematic of PCM sample contained in a pan for lab-scale DSC analysis. The volume (V) of a PCM sample for DSC is typically less than 100 μL, which makes the Biot number (Bi) less than 0.1 and the temperature (T) distribution of the PCM spatially uniform. (b) A schematic of PCM-embedded building envelopes. PCMs in system-scale applications such as buildings, on the other hand, typically have much larger volume that results in Bi much higher than 0.1 and spatially non-uniform temperature distribution of the PCM. Color gradients in the schematic represents the non-uniform temperature distribution. (c) The literature data of θ_s of $MgCl_2 \cdot 6H_2O$ as a function of volume.[13-23] Generally, θ_s decreases with volume; however, limited understanding of the effects of size and thermal conditions on θ_s makes

the relationship between the lab-scale and system-scale θ_s unclear. All data used in this plot are summarized in the Supplemental Information Table S1.

Recently, a methodology was proposed by our group that enabled the prediction of θ_s for a large-scale PCM based on the lab-scale characterization with DSC analysis. The proposed methodology was validated on solid-solid phase change of neopentyl glycol (NPG) with a very simple rod-like geometry.[27] The solid-solid phase change, however, has been relatively less-explored for TES applications due to its relatively low latent heat, leaving the supercooling issue of solid-liquid PCMs unresolved. In this work, we validate the methodology with general PCMs; that is, we demonstrate that θ_s of solid-liquid phase change can be predicted for PCMs with arbitrary geometry and thermal conditions. To investigate the applicability of our approach for multiple material types, we first characterized the nucleation behaviors for two types of PCMs: an organic and an inorganic material, in this case, a fatty acid and a salt hydrate. Fatty acids are, like paraffins, organic materials, and their phase change depends on the crystallization of hydrocarbon chains. Fatty acids have shown potential for TES with great chemical stability and reproducibility over long thermal cycles.[9] Salt hydrates, which are inorganic compounds, have great thermo-physical properties for TES applications, e.g., high latent heat of fusion, thermal conductivity, and density; however, salt hydrates experience significant supercooling, limiting the use of them for TES despite the great thermo-physical properties.[9] Here, we tested decanoic acid (also known as capric acid) and $MgCl_2 \cdot 6H_2O$ for the study of fatty acids and salt hydrates, respectively. Based on the statistical analysis of θ_s values from more than one hundred heating-cooling cycles using DSC, we show that nucleation behaviors of both material types can be characterized by a non-homogeneous Poisson distribution. With the statistical characterization of nucleation, we demonstrate the θ_s prediction for large-scale $MgCl_2 \cdot 6H_2O$ samples under both isothermal and non-isothermal conditions. The experimental results showed excellent agreement with our prediction. This work can provide guidelines for design optimization of PCM-based applications and, thus, has important implications for the deep decarbonization of global energy use.

STATISTICAL MODELING OF NUCLEATION

The first step to predict the degree of supercooling is to understand the nucleation behavior of a PCM. In fact, θ_s changes for every freezing event due to the stochastic nature of nucleation,

meaning it needs to be described from a statistical point of view. A statistical model, called a non-homogeneous Poisson process, have been successfully used to describe the nucleation of supercooled metals and precipitation of supersaturated solutions.[28-33] Here, we use it to describe the supercooling of PCMs for TES applications. Note that "non-homogeneous" used here is irrelevant to the nucleation being homogeneous or heterogeneous; instead it is a purely statistical term that means the rate parameter of Poisson process can vary in time (t), which will be explained further below.

There are two important functions that describe the nucleation distribution in time: the survival function ($\chi(t)$) and the probability distribution function (PDF, $f(t)$). For nucleation, the survival function describes the probability that a nucleation site will survive (non-nucleated) over a certain period of time and can be expressed as

$$\chi(t) = e^{-\int_0^t J(\tau)d\tau}. \quad (1)$$

Here J is the Poisson rate parameter which is equivalent to the PCM-wide nucleation rate at time t. For most TES applications, PCMs go through the change in temperature (T), which may change the nucleation rate (J) over time, so the nucleation is modeled as a "non-homogeneous" Poisson process, as opposed to a homogeneous Poisson process with a constant nucleation rate. Note that, instead of the survival function, a cumulative distribution function (CDF, $F(t)$) can be used, which simply describes the opposite case of the survival function – a probability that a nucleation site will nucleate over the period of time t – and be expressed as $F(t) = 1 - \chi(t)$. Then, a PDF can be obtained as the derivative of the CDF, i.e.,

$$f(t) = \frac{\mathrm{d}F}{\mathrm{d}t} = \frac{\mathrm{d}(1-\chi)}{\mathrm{d}t}. \quad (2)$$

The PDF shows the probability of nucleation at any nucleation site at time t; therefore, the expected time for the PCM-wide first nucleation (t_{avg}) can be derived from the first moment (mean) of the PDF, i.e.,

$$t_{\mathrm{avg}} = \int_0^\infty tF(t)dt. \quad (3)$$

Likewise, the standard deviation (t_{std}) of time for the first nucleation can be derived from the second central moment of the PDF as

$$t_{\mathrm{std}} = \sqrt{\int_0^\infty t^2 F(t)dt - {t_{\mathrm{avg}}}^2}. \quad (4)$$

Once the first nucleation occurs, the phase change cascades from the first nucleation site to all over the PCM.

In general, the PCM-wide nucleation rate scales with the number of nucleation sites in a PCM. Further, because the nucleation rate for a site within the bulk (homogeneous nucleation) and at the surface of a PCM (heterogeneous nucleation) may differ, we can express the overall nucleation rate as the sum of the two, i.e., $J(t) = VJ_V(t) + AJ_A(t)$, where V is the volume and A is the surface area of a PCM, and J_V and J_A are the volume-specific and surface area-specific nucleation rates, respectively. When a PCM is in contact with a functionalized substrate with coatings of nucleating agents [26], heterogeneous nucleation at the interface may dominate the overall nucleation rate. Otherwise, for a PCM in contact with a substrate sharing a chemically stable interface, we can assume that the nucleation will scale with volume and for a sufficiently large system, $J \cong VJ_V$. Throughout this work, we simplify $J \cong VJ_V$ as we used aluminum containers with a chemically-stable passivation coating on the surface.

RESULTS

Characterization of Nucleation

Now we modify the statistical modeling of nucleation for the analysis of DSC data. We first need to characterize the nucleation rate as a function of temperature rather than time, so that we can evaluate the nucleation rate of a PCM under a certain temperature. The change of variables from time to temperature can be simply done such that $T(t) = T$ with the initial condition at T_{m} as $T(t = 0) = T_{\mathrm{m}}$. Further, in a DSC study, a sample is typically thermally lumped and cools at a constant rate. Therefore, it is convenient to define the cooling rate (β) to be a positive number such that $\frac{\mathrm{d}T}{\mathrm{d}t} = -\beta$. Consequently, we can express the survival function (Equation (1)) and PDF (Equation (2)) with an independent variable of θ_{s} as

$$\chi(\theta_{\mathrm{s}}) = e^{-\frac{V}{\beta}\int_0^{\theta_{\mathrm{s}}} J_{\mathrm{V}}(\theta_{\mathrm{s}}')d\theta_{\mathrm{s}}'} \text{ and} \quad (5)$$

$$f(\theta_{\mathrm{s}}) = \frac{V}{\beta} J_{\mathrm{V}} e^{-\frac{V}{\beta}\int_0^{\theta_{\mathrm{s}}} J_{\mathrm{V}}(\theta_{\mathrm{s}}')d\theta_{\mathrm{s}}'}. \quad (6)$$

From the statistical distribution, we can obtain the volume-specific nucleation rate as a function of the degree of supercooling by rearranging Equation (5) as

$$J_{\mathrm{V}}(\theta_{\mathrm{s}}) = -\frac{\beta}{V}\frac{1}{\chi}\frac{d\chi}{d\theta_{\mathrm{s}}}. \quad (7)$$

With Equation (7), we can obtain empirical data points of $J_{\mathrm{V}}(\theta_{\mathrm{s}})$ characterized by DSC analysis. Then, we fit $J_{\mathrm{V}}(\theta_{\mathrm{s}})$ to a power law function, following the general form of a rate equation in the classical nucleation theory, with two fitting parameters of γ and n as

$$J_{\mathrm{V}}(\theta_{\mathrm{s}}) = \gamma {\theta_{\mathrm{s}}}^{n}.^{27,34} \quad (8)$$

Here the pre-exponential factor γ captures the volumetric number density of nucleation sites and growth rate of molecules at a nucleus and the exponent n dictates the energy barrier for nucleation.[28,35] With two empirical parameters (γ and n), Equation (8) allows us to evaluate the volume-specific nucleation rate as a sole function of θ_{s}. The survival function and probability distribution function can also be expressed with the fitting parameters by replacing J_{V} in the equations as

$$\chi(\theta_{\mathrm{s}}) = e^{-\frac{\gamma V}{\beta(n+1)}{\theta_{\mathrm{s}}}^{(n+1)}} \text{ and} \quad (9)$$

$$f(\theta_{\mathrm{s}}) = \frac{\gamma V}{\beta}{\theta_{\mathrm{s}}}^{n} e^{-\frac{\gamma V}{\beta(n+1)}{\theta_{\mathrm{s}}}^{(n+1)}}. \quad (10)$$

Subsequently, we experimentally characterized the nucleation of $MgCl_2 \cdot 6H_2O$ (255777, Sigma Aldrich) and decanoic acid (21409, Sigma Aldrich) using DSC and plotted $\chi(\theta_{\mathrm{s}})$, $f(\theta_{\mathrm{s}})$, and $J_{\mathrm{V}}(\theta_{\mathrm{s}})$ in **Figure 2**. For each material, we collected data for three conditions by changing the mass (m) and β to investigate the effects of sample size and cooling rate on θ_{s}. For example, in the case of $MgCl_2 \cdot 6H_2O$ (Figure 2(a – c)), Sample 1 (blue) and Sample 2 (red) have different m of 1.4 and 19.8 mg, respectively, but the same β of 10 °C/min. Similarly, Sample 2 (red) and Sample 3 (yellow) have the same m of 19.8 mg but different β of 10 and 1 °C/min, respectively. We ran 150 and 120 heating-cooling cycles for each sample of $MgCl_2 \cdot 6H_2O$ and decanoic acid, respectively; the heating rate was the same for all samples as 10 °C/min. The T_{m} of $MgCl_2 \cdot 6H_2O$ and decanoic acid were 115.2 and 29.7 °C, respectively, and were measured with DSC by the intersection of the baseline heat flow and the tangential line of the melting peak. Then T_{f} of each cooling cycle was determined as the temperature at the first deviation point of the baseline heat flow, where the deviation was caused by the immediate discharge of heat by freezing, a phenomenon also known as recalescence. With the measured T_{f} and T_{m}, we obtained θ_{s} for each cycle and calculated $\chi(\theta_{\mathrm{s}})$ by counting the number of non-nucleated cycles at a certain θ_{s} and

dividing by the total number of cycles. Likewise, by counting the number of cycle nucleating at θ_s, we calculated the $f(\theta_s)$. Finally, $J_V(\theta_s)$ was obtained by converting $\chi(\theta_s)$ using Equation (1). Solid lines in the plots are fitting results based on Equation (2), where the good fits with experimental data validates the simplification of J_V with two parameters of γ and n.

The results of $MgCl_2 \cdot 6H_2O$ clearly show the effects of sample size and cooling rate on θ_s in Figure 2 (a) and 2(b). $MgCl_2 \cdot 6H_2O$ samples show a wide spread of θ_s, ranging from ≈ 15 to 40 °C. Compared to Sample 1 (blue), both $\chi(\theta_s)$ and $f(\theta_s)$ of Sample 2 (red) shifted to the left, indicating the decrease in θ_s with increase in the sample size for the same cooling rate. Likewise, the slower cooling rate of Sample 3 (yellow) resulted in the left-shift of $\chi(\theta_s)$ and $f(\theta_s)$ of Sample 3 compared to those of Sample 2 (red) for the same sample size. The results are consistent with our qualitative understanding, that is, θ_s decreases with the increase in sample size and decrease in cooling rate. Specifically, a larger sample has a higher probability for nucleation as it has spatially more nucleation sites. Likewise, a slower cooling rate results in a higher probability for nucleation because there are more nucleation attempts. We found a similar result regarding the sample size with decanoic acid, that is, the decreased θ_s with the increase in m (Sample 1 and Sample 2). The effect of cooling rate, however, was not obvious for decanoic acid. For example, Sample 2 (red) showed a very close θ_s distribution with Sample 3 (yellow) with a ten-times slower cooling rate. We presume the very similar θ_s of Sample 2 and Sample 3 is because the θ_s of Sample 2 is already very small (ranging from $\approx 2 - 5.5$ °C), leaving less space for the further decrease with the slower β. In fact, the $f(\theta_s)$ of Sample 3 shows a slightly lower θ_s than Sample 2, which can be found from the longer tail for small θ_s down to ≈ 1.5 °C. Finally, we plotted all the data points of nucleation rate as a function of θ_s and fitted them with Equation (8), resulting in $\gamma = 3.17 \times 10^{-10}$ °C^{-n}min^{-1}m^{-3} and $n = 12.38$ for $MgCl_2 \cdot 6H_2O$ (Figure 2(c)) and $\gamma = 4.85 \times 10^{-4}$ °C^{-n}min^{-1}m^{-3} and $n = 6.44$ for decanoic acid (Figure 2(f)).

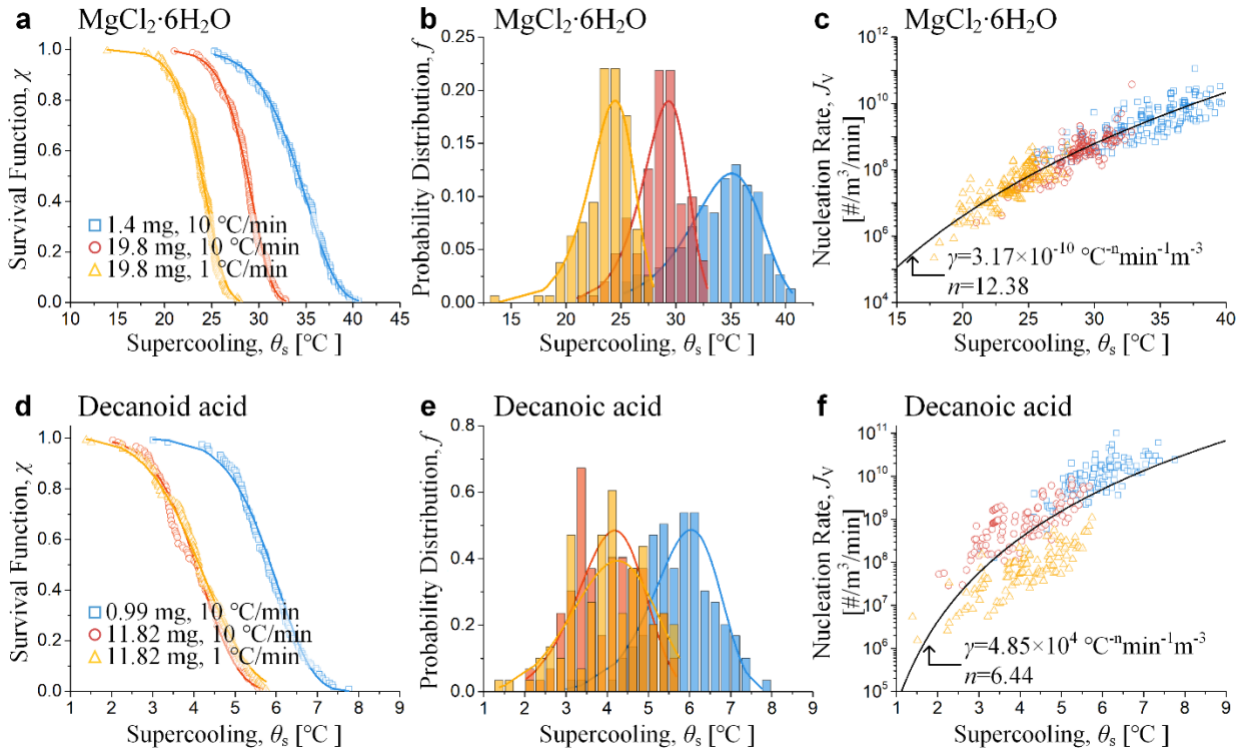

Figure 2. Statistical distributions of θ_s and nucleation rates of $MgCl_2 \cdot 6H_2O$ and decanoic acid obtained by DSC analysis. (a) Survival function and (b) probability distribution function of $MgCl_2 \cdot 6H_2O$ as a function of θ_s. Sample 1 (blue) and Sample 2 (red) have the same β of 10 ℃/min but different *m* of 1.4 and 19.8 mg, respectively. In contrast, Sample 2 (red) and Sample 3 (yellow) have the same *m* of 19.8 mg but different β of 10 and 1 ℃/min, respectively. θ_s distributions of three samples show that θ_s decreased with the increase of *m* and decrease of β. Data points are experimental data. Solid lines show the fitting results of the experimental data with the power law function of J_V. (c) Volume-specific nucleation rate J_V of $MgCl_2 \cdot 6H_2O$ calculated from the survival function. Fitting (black solid line) of all experimental data with the power law $J_V(\theta_s) = \gamma \theta_s^{\,n}$ results in $\gamma = 3.17 \times 10^{-10}$ $℃^{-n}$ $\mathrm{min^{-1}m^{-3}}$ and $n = 12.38$. (d) Survival function and (3) probability distribution function of decanoic acid. Sample 1 (blue), Sample 2 (red), and Sample 3 (yellow) have *m* of 0.99, 11.82, and 11.82 mg and β of 10, 10, and 1 ℃/min, respectively. While the decrease of θ_s from Sample 2 to Sample 3 by the decrease of β is not as apparent as $MgCl_2 \cdot 6H_2O$, a similar decreasing trend of θ_s was found with the increase of

m. (f) J_V of decanoic acid calculated from the survival function. The black solid line shows the power-law fit of experimental data with $\gamma = 4.85 \times 10^4$ ℃$^{-n}$ min^{-1}m^{-3} and $n = 6.44$.

Prediction of θ_s of large volume with uniform temperature

For a large system with Biot number (Bi) less than 0.1, e.g., thin slabs or cylinders, we can approximate that the system has a spatially uniform temperature distribution, i.e., lumped thermal capacitance. For this special case, we can derive the average degree of supercooling ($\theta_{s,avg}$) and the standard deviation ($\theta_{s,std}$) from the first and second moment of the PDF, respectively, as $\theta_{s,avg}(V,\beta) = \int_0^\infty \theta_s f(\theta_s) d\theta_s$ and $\theta_{s,std}(V,\beta) = \sqrt{\int_0^\infty {\theta_s}^2 f(\theta_s) d\theta_s - {\theta_{s,avg}}^2}$. This yields to

$$\theta_{s,avg}(V,\beta) = \beta^{\frac{1}{n+1}} \left(\frac{n+1}{\gamma V}\right)^{\frac{1}{n+1}} \Gamma\left(\frac{n+2}{n+1}\right) \text{ and} \quad (11)$$

$$\theta_{s,std}(V,\beta) = \beta^{\frac{1}{n+1}} \left(\frac{n+1}{\gamma V}\right)^{\frac{1}{n+1}} \left\{\Gamma\left(\frac{n+3}{n+1}\right) - \left[\Gamma\left(\frac{n+2}{n+1}\right)\right]^2\right\}^{1/2}, \quad (12)$$

where Γ is the gamma function [27,33].

To validate our prediction of Equation (11) and (12), we performed large-scale experiments for $MgCl_2 \cdot 6H_2O$ in an oven (**Figure 3a**). We first filled two different masses (265.7 and 1776 mg) of $MgCl_2 \cdot 6H_2O$ in a tubing made of the same material (Alodine®-coated aluminum) as a pan and lid used for DSC. This mass is up to two orders of magnitude higher than that used in DSC. The inner and outer diameters of the tubing were 5.24 and 5.95 mm, respectively. The Bi of $MgCl_2 \cdot 6H_2O$ in the tubing can be evaluated as $Bi = \frac{d_{PCM}/k_{PCM}}{(t_{Al}/k_{Al})+(1/h)}$, where d_{PCM}, k_{PCM}, t_{Al}, k_{Al}, and h are the diameter and thermal conductivity of $MgCl_2 \cdot 6H_2O$, aluminum tubing wall thickness, aluminum thermal conductivity, and convection heat transfer coefficient. Because of the small wall thickness (t_{Al} of 0.355 mm) and high thermal conductivity of aluminum (k_{Al} ≈170 W/mK), we can neglect t_{Al}/k_{Al} compared with $1/h$ in the denominator as $Bi \cong \frac{d_{PCM}/k_{PCM}}{(1/h)}$. d_{PCM} is equivalent to the inner diameter of tubing (5.24 mm) and the thermal conductivity of liquid phase $MgCl_2 \cdot 6H_2O$ (≈ 0.570 W/mK) is used for k_{PCM} [15]. For a typical h value of 10 W/m^{2}K, the Bi is less than 0.1. Four thermocouples were attached to the outer wall of the tubing to detect the phase change from a sudden change in temperature. The tubing was vertically hung in the oven and tested

at two different β of 8 and 0.1 °C/min. We tested 25 cooling cycles for the β of 8 °C/min and 6 cooling cycles for the β of 0.1 °C/min.

We compared our prediction based on Equation (3) with experimental results of oven tests (squares) along with DSC data (circles) in Figure 3b. The black solid line indicates the equivalence between the prediction and experiments and grey dashed lines show the ±20% deviation range. We evaluated the uncertainty of prediction using the Dvoretzky-Kiefer-Wolfowitz-Massart inequality (DKW inequality) and represented the uncertainty as error bars in the plot (detailed uncertainty analysis is available in Section II of Supplemental Information). The DKW inequality is a probability theorem that provides upper and lower bounds on the maximum difference between the empirically measured distribution function and the true cumulative distribution function of the underlying probability distribution function.[36] Error bars for experimental data represent standard deviations. For all cases, experimental data showed an excellent agreement with our prediction. Also, the oven tests confirmed the dependency of θ_s on the system size and β again – larger oven samples showed lower θ_s values than DSC samples and the β of 0.1 °C/min resulted in a lower θ_s compared to the β of 8 °C/min.

Figure 3c and 3d show the average and standard deviation of θ_s of $MgCl_2 \cdot 6H_2O$ using Equation (3) and (4) with γ and n values obtained from the DSC analysis. The plots clearly show that both average and standard deviation of θ_s decrease with increasing volume and decreasing cooling rate, with the scaling relationship as $\sim V^{-\frac{1}{n+1}}$ and $\sim \beta^{\frac{1}{n+1}}$. These contour maps can serve as *a priori* design guidelines for the optimization of PCM-based applications.

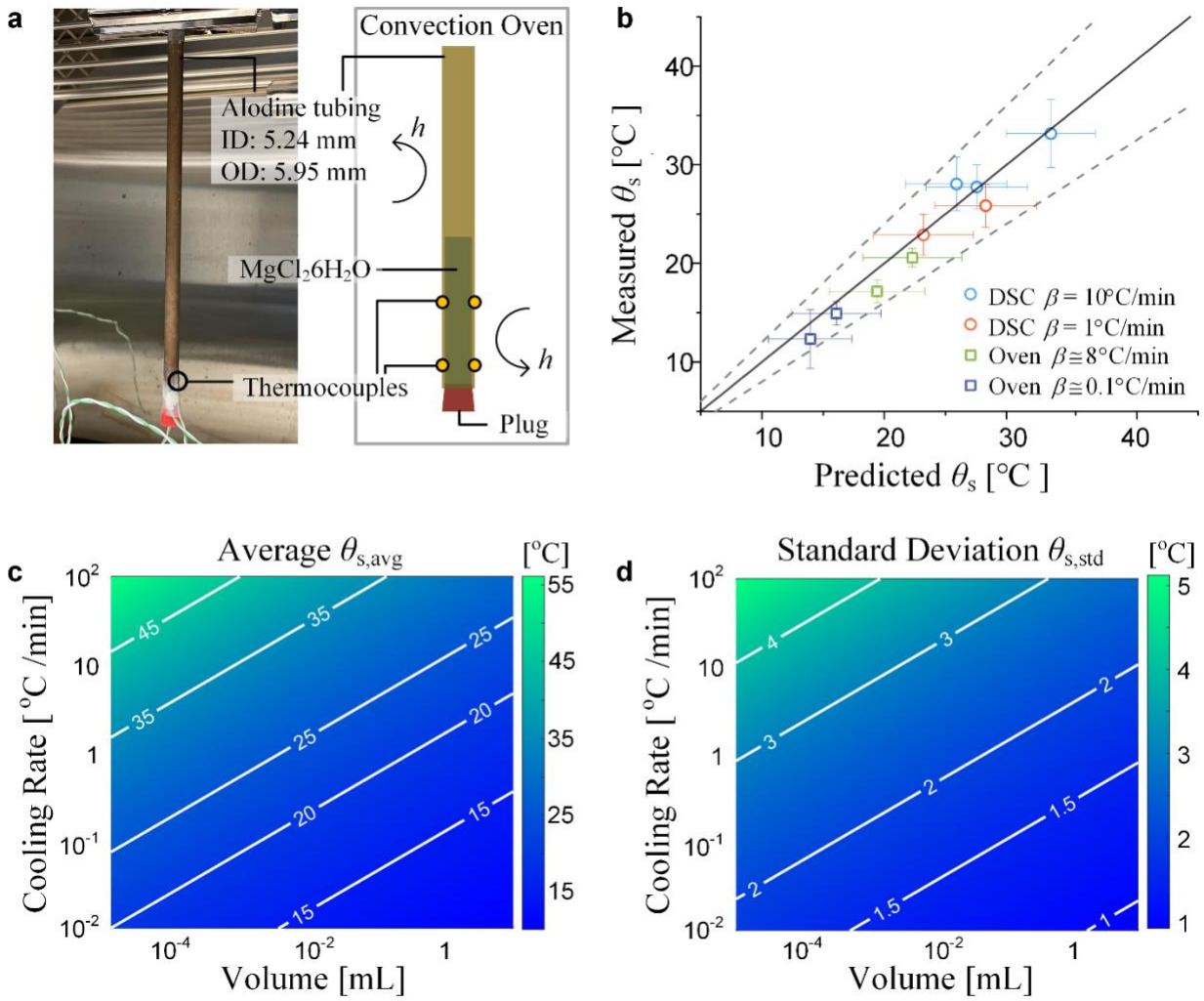

Figure 3. Prediction of θ_s for lumped thermal capacitance cases. (a) Experimental setup to measure θ_s values of large but lumped thermal capacitance samples. An Alodine®-coated aluminum tubing was filled with $MgCl_2 \cdot 6H_2O$ and vertically hung in an oven. Tubing dimensions were chosen to make sure the Bi of $MgCl_2 \cdot 6H_2O$ in the tubing is less than 0.1. Two different m (265.7 and 1776 mg) and β (8 and 0.1 ℃/min) were tested. Four thermocouples were attached to the outer wall to detect the phase change. (b) Experimental results of θ_s values (y-axis) measured for large samples in an oven (squares) as well as DSC samples (circles) compared with our prediction (x-axis). A black solid line indicates the equivalence of experiments and prediction. Grey dashed lines show the ±20% deviation range. Error bars for prediction were evaluated based on the DKW analysis with the 90% confidence level (further details in Section II of Supplemental

Information). Error bars for experimental data are standard deviations of measurements. (c) Contour maps of average and (d) standard deviation of θ_s as a function of V and β in log-log scale. Both the average and standard deviation follow the scaling relationship with V and β as $\sim V^{-\frac{1}{n+1}}$ and $\sim \beta^{\frac{1}{n+1}}$.

Prediction of t_{avg} for General Case

For most systems with arbitrary geometry and thermal conditions, the temperature distribution within a PCM is non-uniform, meaning that a single temperature cannot be defined for the whole system. For this general case, therefore, we predict the expected time (t_{avg}), instead of θ_s, for a PCM to nucleate. First, we obtain the temperature distribution across the PCM over the period of cooling time for a given geometry and thermal conditions through a numerical simulation. The temperature distribution is then converted to the nucleation rate distribution using the power-law relationship $J_V(\theta_s) = \gamma {\theta_s}^n$. Each finite volume element in the PCM is assigned to a specific nucleation rate that changes in time ($J_{V,i}(\vec{x}, t)$, where $J_{V,i}$ and $\vec{x}$ are the volume-specific nucleation rate and position vector of a finite volume element, respectively). Finally, the global nucleation rate (J) over the PCM can be simply obtained as the sum of the nucleation rate of each element [27,37]. This conversion from the temperature distribution to the global nucleation rate can be expressed as

$$J(t) = \iiint J_{V,i}(\vec{x}, t)\mathrm{d}V = \iiint \gamma {\theta_{s,i}}^n(\vec{x}, t)\mathrm{d}V, \quad (13)$$

where $\theta_{s,i}$ and $\mathrm{d}V$ are the degree of supercooling and volume of each finite element, respectively. With the global nucleation rate, the PCM-wide survival function and PDF can be evaluated using Equation (1) and (2), respectively; subsequently, the expected time (t_{avg}) and standard deviation (t_{std}) for the first nucleation can be calculated with Equation (3) and (4), respectively.

To test our prediction for a non-uniform temperature case, we fabricated an aluminum plate-fin heat exchanger and embedded 31 g of $MgCl_2 \cdot 6H_2O$ between the fins (**Figure 4a**). To prevent corrosion, the entire surface of the heat exchanger was covered with a roughly 500-nm-thick Parylene C layer deposited by chemical vapor deposition. The length (l), width (w), and height (h) of the fins were 30, 3, and 15 mm, respectively. The gap between the fins was 12 mm. We also created four 15 mm-deep holes in two fins and inserted thermocouples to measure temperature change and detect a phase change. After embedding the $MgCl_2 \cdot 6H_2O$ between the

fins, we covered the heat exchanger with a lid and sealed the gap between the lid and heat exchanger using Teflon tape to prevent the loss of vapor. The whole device including the lid had a width of 93 mm, depth of 39 mm, and height of 24.4 mm. We put the PCM-embedded heat exchanger in an oven at 130 ℃ for ≈ 210 min to melt $MgCl_2 \cdot 6H_2O$ and thermalize the whole device. Then, we took the heat exchanger out and cooled it down at room temperature by natural convection to freeze $MgCl_2 \cdot 6H_2O$ (Figure 4b). We ran eight heating-cooling cycles; on average, the first nucleation occurred in 327 sec with a standard deviation of 41.5 sec. Figure 4c shows the temperature change of the first heating-cooling cycle, where a temperature plateau between 45 and 67 min shows the melting, and a temperature spike around 228 min indicates the freezing of $MgCl_2 \cdot 6H_2O$.

To get the temperature distribution for θ_s prediction, we applied the same conditions for a numerical simulation using COMSOL, that is, the initial temperature condition of 130 ℃ and cooling by natural convection. The density, heat capacity, and thermal conductivity of $MgCl_2 \cdot 6H_2O$ were set to be 1460 kg/m^3, 2250 J/(kg·K), and 0.570 W/(m·K), respectively [15,38,39]. The heat transfer coefficients for natural convection of sidewalls, top, and bottom surfaces were set as 12, 8.8, and 6.6 W/(m^2·K), respectively, which were measured by separate experiments. Figure 4d shows the resulting temperature distribution of the $MgCl_2 \cdot 6H_2O$ with a horizontal slice-view after 354 sec of cooling. We then calculated the global nucleation rate in time by taking the volume integral of temperature using Equation (13), from which we obtained the PDF using Equation (2). Figure 4e shows the resulting PDF in time with t_{avg} at 354.3 sec (red vertical line) and t_{std} of 18.1 sec (red shadow region). Compared with experimental results (327 ± 41.5 sec), our prediction (354.3 ± 18.1 sec) shows an excellent agreement with only ≈ 8% deviation. As an example, we compared our prediction with the freezing point of the first cooling experiment in Figure 4f. Figure 4f shows the temperatures measured by four thermocouples during the cooling period of Figure 4c along with our prediction of t_{avg} (red vertical line) and t_{std} (red shadow region). In this case, the nucleation occurred at 358 sec with only 4 sec difference from our prediction. The excellent agreement with experimental measurements confirms the prediction capability of our framework for a system with an arbitrary geometry and thermal conditions.

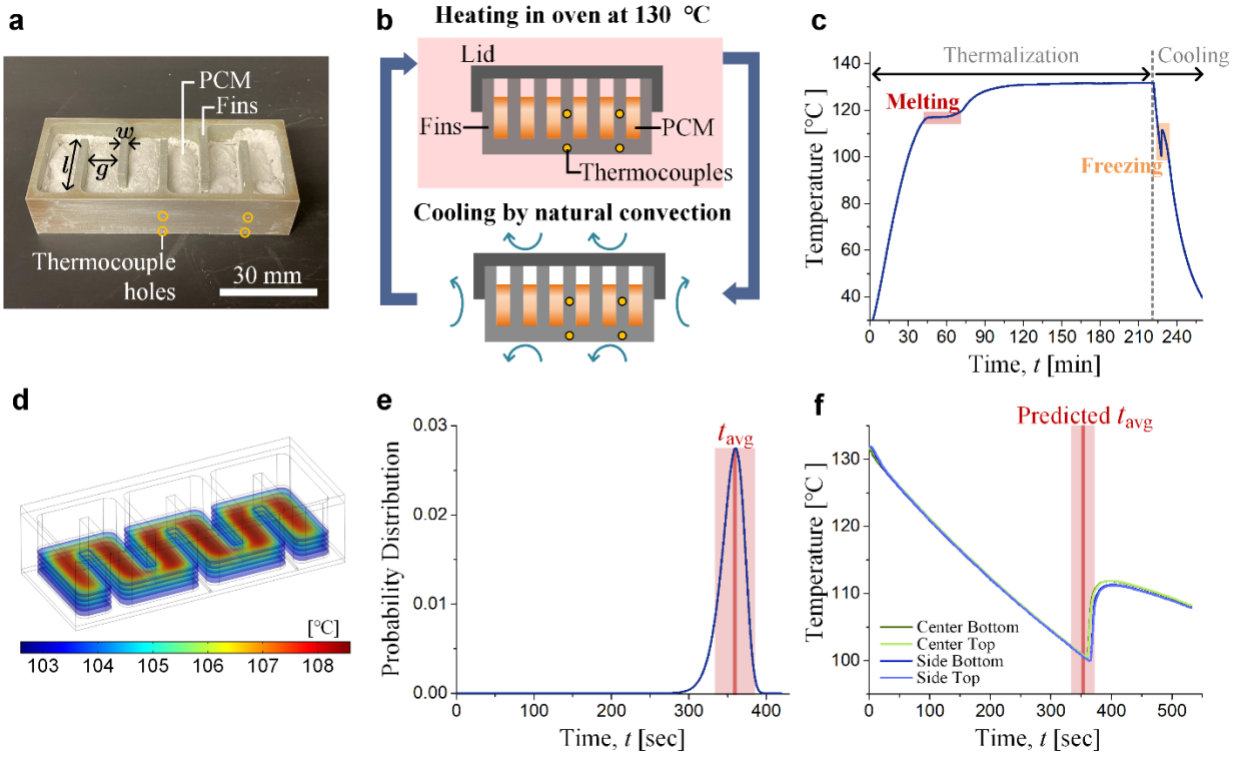

Figure 4. Prediction of t_{avg} and experimental validation for a PCM ($MgCl_2 \cdot 6H_2O$) with non-uniform temperature distribution. (a) A PCM-embedded plate-fin heat exchanger. The heat exchanger is made of aluminum with ≈ 50-nm-thick Parylene C covering the entire surface to protect from corrosion. Four thermocouples were inserted into the fins to measure the temperature change. (b) A schematic of heating-cooling cycle experiments. During heating, the PCM melts and the whole device thermalizes at 130 ℃ in an oven; then, the device was cooled at room temperature by natural convection for nucleation. (c) A temperature profile of a heating-cooling cycle measured by embedded thermocouples. The red shadow region between 45 and 67 min shows the phase transition from solid to liquid at the melting temperature, and the yellow shadow region around 228 min shows the temperature spike due to the freezing. (d) A COMSOL simulation of temperature distribution in the PCM after 354 sec of cooling from the initial temperature of 130 ℃. (3) A PDF of nucleation calculated from COMSOL simulation. The t_{avg} for nucleation was calculated as 354.3 sec with the t_{std} of 18.1 sec. (f) Comparison of experimental data of the first cooling experiment with our prediction. Four lines show the temperature profile

measured by thermocouples. The freezing point (temperature spike) at 358 sec shows an excellent agreement with our prediction of 354.3 sec.

DISCUSSION

In this work, we addressed the unclear dependency of the degree of supercooling of general solid-liquid PCMs on their geometrical and thermal conditions with a framework that can predict the degree of supercooling. We first characterized the intrinsic statistical nucleation behavior of PCMs using laboratory-scale DSC experiments. By modeling the nucleation as a non-homogeneous Poisson distribution, we converted the survival function of nucleation to the volume-specific nucleation rate as a function of the degree of supercooling, which, subsequently, was fitted with a power-law function using two fitting parameters γ and n as $J_{\mathrm{V}}(\theta_{\mathrm{s}}) = \gamma {\theta_{\mathrm{s}}}^{n}$. This power-law function allows us to evaluate the PCM-wide nucleation rate for given geometrical and thermal conditions of a PCM. For a lumped thermal capacitance case, our framework could calculate the average degree of supercooling. For an experimental validation, we filled an aluminum tubing with $MgCl_2 \cdot 6H_2O$ and ran heating-cooling cycles in an oven. We measured the degree of supercooling from temperature measurements which showed an excellent agreement with our prediction. We also showed that, for a lumped thermal capacitance case, our framework could draw contour maps of the average and standard deviation of the degree of supercooling as a function of system size and cooling rate, which can serve as a design guideline for an optimized PCM-based system. For a general case with a non-uniform temperature distribution, our framework could evaluate the expected time for nucleation. We first calculated the temperature distribution within the PCM over time through numerical simulation. The temperature distribution was then converted into a PCM-wide global nucleation rate in time and, accordingly, into the expected time for nucleation and its standard deviation. We validated our prediction with heating-cooling experiments of a $MgCl_2 \cdot 6H_2O$-embedded plate-fin heat exchanger. We measured the period of time for nucleation over eight heating-cooling cycles; the first nucleation occurred in 327 ± 41.5 sec, which shows an accurate agreement with our prediction of 354.3 ± 18.1 sec. Based on simple laboratory-scale experiments, our framework enables the prediction of supercooling performance for an arbitrarily-shaped PCM under random thermal conditions, which has important implications for improved PCM designs for a variety of applications such as TES for buildings or industrial processes.

EXPERIMENTAL PROCEDURES

Resource Availability

Please contact the lead contacts, S.K (skaur1@lbl.gov) or R.S.P. (rsprasher@lbl.gov) for information related to the data described in the following experimental procedures section.

DSC Sample Preparation and Measurement

The weight of a DSC pan (Tzero Alodined Pan, TA Instruments) plus a lid (Tzero Hermetic Alodined Lid, TA Instruments) was first measured using a microbalance (AD-6 Autobalance, PerkinElmer). We added a PCM sample in the pan and measured the total weight of PCM, pan, and lid. The weight of the PCM sample was then evaluated by the difference between the total weight and the weight of pan plus lid. The PCM-containing pan and lid were then hermetically sealed by a press (Tzero Press, TA Instruments) and placed in a DSC (DSC2500, TA Instruments). In the case of $MgCl_2 \cdot 6H_2O$, 150 heating-cooling cycles were tested between 65 and 130 ℃. In the case of decanoic acid, 120 heating-cooling cycles were tested between 15 and 40 ℃. A heating rate was 10 ℃/min for all cases and two different cooling rates of 1 and 10 ℃/min were tested. The melting temperature of PCMs was measured from the intersection of the baseline heat flow and the tangential line of the melting peak during a heating cycle. The freezing temperature of each cooling cycle was determined as the first deviation point of the baseline heat flow, where the deviation was caused by the immediate discharge of heat by freezing, a phenomenon also known as recalescence. Finally, the degree of supercooling was evaluated as the difference between the melting and freezing temperatures.

Lumped Thermal Capacitance Sample Preparation and Experimental Procedure

An aluminum (Al 6061-T6) tubing with an inner diameter of 5.24 mm and an outer diameter of 5.95 mm was cut into 15-cm-long pieces. To protect the tubing from corrosion, we applied an Alodine® coating to the inner and outer surfaces. [Procedure based on the product description] Lastly, the Alodined surfaces were rinsed with deionized water and dried with air blow. One end of tubing was capped with a tapered plug, and 265.7 or 1776 mg of $MgCl_2 \cdot 6H_2O$ was introduced into the tubing. Then, the other end of the tubing was also capped with the same tapered plug. Both ends with plugs were tightly sealed using a Teflon tape to prevent the loss of vapor. Four K-type thermocouples (SE028, Pico Technology) were attached at the outer surface

to measure the temperature change and detect the phase change temperatures with a thermocouple data logger (TC-08, Pico Technology). The sample was vertically hung in a convection oven. Heating-cooling cycle experiments were performed by cycling temperatures between 87 and 133 °C. The cooling rate was precisely controlled with by a PID temperature controller (F4, Watlow) built in the oven. Two different cooling rates of 0.1 and 8 °C/min were tested. The freezing temperature was measured as the first deviation of a sudden temperature rise from the linear baseline. Uncertainty analysis is available in Section II of Supplemental Information

PCM-embedded Heat Exchanger Preparation and Experimental Procedure

A plate-fin heat exchanger and a lid were fabricated by CNC milling aluminum (Al 6061-T6) blocks. The heat exchanger and the lid were coated with 500nm Parylene C using Chemical Vapor Deposition (CVD). Silane A-174 was used as adhesion promoter for parylene deposition. 31 g of $MgCl_2 \cdot 6H_2O$ filled the gaps between the fins. The top surface of the heat exchanger was covered with the lid and tightly sealed with a Teflon tape to prevent the loss of vapor. Four K-type thermocouples (SCAIN-020G-6, Omega Engineering) were inserted into the fins to measure the temperature change and to detect phase change points. The device was placed in an oven at 130 °C for roughly two and a half hours for thermalization. After thermalization, the device was taken out to the laboratory-ambient and placed on top of two insulation foams at two ends of the device for cooling of all surfaces by natural convection at room temperature. The period of time taken for nucleation was measured from the start of the cooling period to the moment of a sudden temperature rise.

We used experimentally measured heat transfer coefficient (HTC) values in a numerical simulation for prediction. We cut a 1.27-mm-thick aluminum plate into separate pieces that have the same dimensions with the bottom and top surfaces and the sidewalls of the actual plate-fin heat exchanger. Then, the backside of the pieces was covered with an insulation foam to ensure the heat transfer occurs at only one side of the pieces. Subsequently, each piece was thermalized at 130 °C and cooled by natural convection in the same laboratory environment with the heat exchanger was in for the measurement. The temperature (T) change of pieces in time (t) can be expressed as $mc_{\mathrm{p}}\frac{dT}{dt} = -hA(T - T_{amb})$, where m, c_{p}, h, A, and T_{amb} are the mass and specific heat of aluminum, HTC value, exposed surface area, and the ambient temperature. By rearranging and

taking the log of this equation, we have $\log(T - T_{amb}) = \log(T_i - T_{amb}) - \frac{h}{\rho c_p z} t$, where T_i, ρ, and z are the initial temperature, the density of aluminum, and the thickness of the aluminum piece, respectively. Therefore, we can measure the HTC values (h) by measuring the slope of $\log(T - T_{amb})$ in time. The measured h values for top and bottom surfaces and the side walls are 8.79, 6.64, and 11.95 W/m^{2}K, respectively.

Numerical Analysis of Nucleation Rate Distribution

We calculated the nucleation rate distribution and its change over time through numerical simulation using COMSOL. We created the geometry of the PCM-embedded heat exchanger in COMSOL, identical to the actual device. Material properties of aluminum 6061-T6 were used for the heat exchanger. For the embedded $MgCl_2 \cdot 6H_2O$, we defined the density, heat capacity, and thermal conductivity as 1460 kg/m^3, 2250 J/(kg·K), and 0.570 W/(m·K), respectively. We used the 'Heat Transfer in Solids' module. The initial temperature of the entire device was set to 130 °C. We applied the measured heat transfer coefficient (h) values for top and bottom surfaces and the side walls, which are 8.79, 6.64, and 11.95 W/m^{2}K, respectively. We created physics-controlled meshes with the extra fine element size, creating mostly tetrahedra meshes with some triangle meshes. The average element quality was 0.6574 and the maximum and minimum element sizes were 9.3 mm and 1.6 mm, respectively. We then calculated the change in temperature distribution over time, using a time step of 2 seconds for 10 minutes. Finally, the resulting temperature distribution was converted into a nucleation rate distribution, using the power law function, i.e., $J_V(\theta_s) = \gamma {\theta_s}^n$, with $\gamma = 3.17 \times 10^{-10}$ °C^{-n}min^{-1}m^{-3} and $n = 12.38$.

SUPLLEMENTAL INFORMATION

Supplemental Information can be found online at

ACKNOWLEDGMENT

The authors gratefully acknowledge the support and funding for this research provided by Energy Efficiency and Renewable Energy, Building Technologies Program, of the U.S. Department of Energy under Contract No. DEAC02-05CH11231.

AUTHOR CONTRIBUTIONS

Conceptualization, Y.S., D.L, S.K., and R.S.P.; Methodology, Y.S. and D. L.; Formal Analysis, Y.S. and D.L.; Investigation, Y.S. and D.C.; Writing – Original Draft, Y.S. and R.S.P. Writing – Review & Editing, Y.S., D.L., D.C., S.K., and R.S.P.; Visualization, Y.S.; Supervision, R.S.P.; Project Administration, S.K. and R.S.P.; Funding Acquisition, S.K. and R.S.P.

DECLARATION OF INTERESTS

The authors declare no competing interests.

INCLUSION AND DIVERSITY STATEMENT

We support inclusive, diverse, and equitable conduct of research

REFERENCES

1. Gilbert, T., Menon, A.K., Dames, C., and Prasher, R. (2023). Heat source and application-dependent levelized cost of decarbonized heat. Joule *7*, 128-149.
2. Amy, C., Seyf, H.R., Steiner, M.A., Friedman, D.J., and Henry, A. (2019). Thermal energy grid storage using multi-junction photovoltaics. Energy Environ. Sci. *12*, 334-343.
3. Kim, J., Oh, J., and Lee, H. (2019). Review on battery thermal management system for electric vehicles. Appl. Therm. Eng. *149*, 192-212.
4. Kandasamy, R., Wang, X.-Q., and Mujumdar, A.S. (2008). Transient cooling of electronics using phase change material (PCM)-based heat sinks. Appl. Therm. Eng. *28*, 1047-1057.
5. Hasan, A., McCormack, S.J., Huang, M.J., and Norton, B. (2014). Energy and Cost Saving of a Photovoltaic-Phase Change Materials (PV-PCM) System through Temperature Regulation and Performance Enhancement of Photovoltaics. Energies *7*, 1318-1331.
6. Yang, T., King, W.P., and Miljkovic, N. (2021). Phase change material-based thermal energy storage. Cell Rep. Phys. Sci. *2*, 100540.
7. Gur, I., Sawyer, K., and Prasher, R. (2012). Searching for a Better Thermal Battery. Science *335*, 1454-1455.
8. Sharma, A., Tyagi, V.V., Chen, C.R., and Buddhi, D. (2009). Review on thermal energy storage with phase change materials and applications. Renewable and Sustainable Energy Reviews *13*, 318-345.

9. Safari, A., Saidur, R., Sulaiman, F.A., Xu, Y., and Dong, J. (2017). A review on supercooling of Phase Change Materials in thermal energy storage systems. Renewable and Sustainable Energy Reviews *70*, 905-919.
10. Shao, X.-F., Wang, C., Yang, Y.-J., Feng, B., Zhu, Z.-Q., Wang, W.-J., Zeng, Y., and Fan, L.-W. (2018). Screening of sugar alcohols and their binary eutectic mixtures as phase change materials for low-to-medium temperature latent heat storage. (Ⅰ): Non-isothermal melting and crystallization behaviors. Energy *160*, 1078-1090.
11. Inoue, A. (2000). Stabilization of metallic supercooled liquid and bulk amorphous alloys. Acta Mater. *48*, 279-306.
12. Malakooti, M.H., Kazem, N., Yan, J., Pan, C., Markvicka, E.J., Matyjaszewski, K., and Majidi, C. (2019). Liquid Metal Supercooling for Low-Temperature Thermoelectric Wearables. Adv. Funct. Mater. *29*, 1906098.
13. El-Sebaii, A.A., Al-Amir, S., Al-Marzouki, F.M., Faidah, A.S., Al-Ghamdi, A.A., and Al-Heniti, S. (2009). Fast thermal cycling of acetanilide and magnesium chloride hexahydrate for indoor solar cooking. Energy Convers. Manage. *50*, 3104-3111.
14. El-Sebaii, A.A., Al-Heniti, S., Al-Agel, F., Al-Ghamdi, A.A., and Al-Marzouki, F. (2011). One thousand thermal cycles of magnesium chloride hexahydrate as a promising PCM for indoor solar cooking. Energy Convers. Manage. *52*, 1771-1777.
15. Höhlein, S., König-Haagen, A., and Brüggemann, D. (2017). Thermophysical Characterization of MgCl2·6H2O, Xylitol and Erythritol as Phase Change Materials (PCM) for Latent Heat Thermal Energy Storage (LHTES). Materials *10*, 444.
16. Pilar, R., Svoboda, L., Honcova, P., and Oravova, L. (2012). Study of magnesium chloride hexahydrate as heat storage material. Thermochim. Acta *546*, 81-86.
17. Sun, W., Zhou, Y., Feng, J., Fang, X., Ling, Z., and Zhang, Z. (2019). Compounding MgCl2·6H2O with NH4Al(SO4)2·12H2O or KAl(SO4)2·12H2O to Obtain Binary Hydrated Salts as High-Performance Phase Change Materials. Molecules *24*, 363.
18. Kubota, M., Ona, E.P., Watanabe, F., Matsuda, H., Hidaka, H., and Kakiuchi, H. (2007). Studies on Phase Change Characteristics of Binary Mixtures of Erythritol and MgCl2·6H2O. Journal of Chemical Engineering of Japan *40*, 80-84.
19. Rathgeber, C., Miró, L., Cabeza, L.F., and Hiebler, S. (2014). Measurement of enthalpy curves of phase change materials via DSC and T-History: When are both methods needed to estimate the behaviour of the bulk material in applications? Thermochim. Acta *596*, 79-88.
20. Cantor, S. (1979). DSC study of melting and solidification of salt hydrates. Thermochim. Acta *33*, 69-86.
21. Honcová, P., Sádovská, G., Pastvová, J., Koštál, P., Seidel, J., Sazama, P., and Pilař, R. (2021). Improvement of thermal energy accumulation by incorporation of carbon nanomaterial into magnesium chloride hexahydrate and magnesium nitrate hexahydrate. Renewable Energy *168*, 1015-1026.
22. Lane, G.A. (1992). Phase change materials for energy storage nucleation to prevent supercooling. Sol. Energy Mater. Sol. Cells *27*, 135-160.
23. Ahmed, F., and Waqas, A. (2019). Experimental Investigation Of Using Latent Thermal Energy Storage System Comprising Of Magnesium Chloride Hexahydrate (MgCl2.6H2O) With Domestic Gas Heater. 23-24 Oct. 2019. pp. 1-6.

24. Zahir, M.H., Mohamed, S.A., Saidur, R., and Al-Sulaiman, F.A. (2019). Supercooling of phase-change materials and the techniques used to mitigate the phenomenon. Applied Energy *240*, 793-817.
25. Putri, R.A., Yusuf, A., Rahman, A., Anggraini, Y., Kurnia, D., Wonorahardjo, S., Wonorahardjo, S., and Sutjahja, I.M. (2021). Reduction of the supercooling of Ca(NO3)2•4H2O using electric field and nucleating agent effects. Journal of Energy Storage *42*, 103020.
26. Beaupere, N., Soupremanien, U., and Zalewski, L. (2018). Nucleation triggering methods in supercooled phase change materials (PCM), a review. Thermochim. Acta *670*, 184-201.
27. Lilley, D., Lau, J., Dames, C., Kaur, S., and Prasher, R. (2021). Impact of size and thermal gradient on supercooling of phase change materials for thermal energy storage. Applied Energy *290*, 116635.
28. Wilde, G., Sebright, J.L., and Perepezko, J.H. (2006). Bulk liquid undercooling and nucleation in gold. Acta Mater. *54*, 4759-4769.
29. Bokeloh, J., Rozas, R.E., Horbach, J., and Wilde, G. (2011). Nucleation Barriers for the Liquid-To-Crystal Transition in Ni: Experiment and Simulation. Phys. Rev. Lett. *107*, 145701.
30. Maggioni, G.M., and Mazzotti, M. (2017). Stochasticity in Primary Nucleation: Measuring and Modeling Detection Times. Crystal Growth & Design *17*, 3625-3635.
31. Maggioni, G.M., Bosetti, L., dos Santos, E., and Mazzotti, M. (2017). Statistical Analysis of Series of Detection Time Measurements for the Estimation of Nucleation Rates. Crystal Growth & Design *17*, 5488-5498.
32. Kubota, N., Fujisawa, Y., and Tadaki, T. (1988). Effect of volume on the supercooling temperature for primary nucleation of potassium nitrate from aqueous solution. J. Cryst. Growth *89*, 545-552.
33. Kubota, N. (2012). Effect of sample volume on metastable zone width and induction time. J. Cryst. Growth *345*, 27-33.
34. Kubota, N. (2015). Analysis of the effect of volume on induction time and metastable zone width using a stochastic model. J. Cryst. Growth *418*, 15-24.
35. Sear, R.P. (2007). Nucleation: theory and applications to protein solutions and colloidal suspensions. J. Phys.: Condens. Matter *19*, 033101.
36. Dvoretzky, A., Kiefer, J., and Wolfowitz, J. (1956). Asymptotic Minimax Character of the Sample Distribution Function and of the Classical Multinomial Estimator. The Annals of Mathematical Statistics *27*, 642-669, 628.
37. Kingman, J.F.C. (1992). Poisson Processes (Clarendon Press).
38. Lane, G.A. (2018). Solar Heat Storage: Volume II: Latent Heat Material (CRC Press).
39. Mehling, H., and Cabeza, L.F. (2008). Heat and cold storage with PCM: An up to date introduction into basics and applications (Springer Berlin Heidelberg).